ROYAL SOCIETY
OF CHEMISTRY

PAPER

Check for updates

Reaction mechanism of atomic layer deposition of zirconium oxide using tris(dimethylamino)cyclopentadienyl zirconium: experimental and theoretical study†

Hye-Lee Kim, [ID]‡[ab] Okhyeon Kim, [ID]‡[a] Yong Richard Sriwijaya, [ID][a] Khabib Khumaini, [ID][ac] Romel Hidayat [ID][d] and Won-Jun Lee [ID]★[ab]

We investigated the reaction mechanism of atomic layer deposition (ALD) of zirconium oxide (ZrO_2) by integrating experiments and calculations. The ALD process by alternating the supply of tris(dimethyl-amino)cyclopentadienyl zirconium ($CpZr(NMe_2)_3$) and ozone (O_3) was examined using an *in situ* quartz crystal microbalance (QCM) and the successive surface reaction of the Zr precursor was simulated by density functional theory (DFT) calculations. The QCM analysis suggests that two NMe_2 ligands are released during the first half-cycle of ALD. The DFT calculations indicate that the first two NMe_2 ligands are released during the chemisorption of the Zr precursor with low activation energies of 0.22 eV and 0.16 eV. Conversely, the release of the Cp ligand or the third NMe_2 ligand was unfavorable due to its endothermic nature and high activation energy. Upon completion of the chemisorption of the Zr precursor, the resulting surface species would be $O_2ZrCp(NMe_2)*$, which is in agreement with the QCM results. The integration of the QCM experiment and the DFT calculations is an effective approach to elucidate the ALD reaction mechanism, especially when a heteroleptic precursor is used.

Introduction

One promising approach to developing advanced precursors for atomic layer deposition (ALD) is to create heteroleptic metal–organic compounds in which two or more types of ligands are attached to a metal center.[1–7] These heteroleptic ALD precursors are believed to possess advantages over homoleptic precursors, such as improved thermal stability while maintaining reactivity.[8–11] A notable success was the combination of alkylamide and cyclopentadienyl ligands in a Zr compound to form tris(dimethylamino)cyclopentadienyl zirconium ($CpZr(NMe_2)_3$), which successfully replaced an alkylamide-based homoleptic Zr precursor, tetrakis(ethylmethylamino)zirconium ($Zr(NEtMe)_4$), in the fabrication of dynamic random-access memory (DRAM) devices.[9] In comparison to a homoleptic precursor of $Zr(NEtMe)_4$, $CpZr(NMe_2)_3$ exhibits better thermal stability, resulting in better

a Department of Nanotechnology and Advanced Materials Engineering, Sejong University, Seoul, 05006, Republic of Korea. E-mail: wjlee@sejong.ac.kr

b Metal–organic Compounds Materials Research Center, Sejong University, Seoul, 05006, Republic of Korea

c Department of Chemistry, Universitas Pertamina, Jakarta 12220, Indonesia

d PT PLN, Jakarta 12160, Indonesia

† Electronic supplementary information (ESI) available. See DOI: https://doi.org/10.1039/d4ma00966e

‡ H.-L. Kim and O. Kim are equally contributing first authors.

conformality at a high process temperature of 300 °C with a growth per cycle of ∼0.9 Å.[8]

The ALD process using $CpZr(NMe_2)_3$ and H_2O has been examined by *in situ* quartz crystal microbalance (QCM) at 250 °C.[12] The authors concluded that one Cp ligand per two Zr atoms remains adsorbed at the end of the precursor pulse. However, if this conclusion is correct, the Zr atoms are not sufficiently passivated by the ligands and interact with other Zr precursor molecules, which differs from the ideal ALD process in which the submonolayer grows in a self-limiting manner.

The surface reaction mechanisms of $CpZr(NMe_2)_3$ have also been investigated by density functional theory (DFT) calculations.[13–15] The two successive ligand exchange reactions of $CpZr(NMe_2)_3$ with two surface OH groups were simulated using the $(OH)_2–Si_{21}H_{24}$ cluster model, which mimics hydroxylated Si(100).[13] The reactions were endothermic, making it challenging to elucidate the underlying mechanisms of film growth. In contrast, another study investigated the three successive ligand exchange reactions of $CpZr(NMe_2)_3$ with three surface OH groups using the $(OH)_4–Si_{15}O_{10}H_{16}$ cluster model, which mimics hydroxylated SiO_2.[14] The three reactions, which successively release three $HNMe_2$ molecules, were plausible due to their exothermic nature and low activation energy values. The other study used the $(OH)_4–Si_{15}H_{16}$ cluster model, which mimics the OH-terminated Si(100) surface, and also claimed

that three ligand exchange reactions were exothermic, releasing three $HNMe_2$ molecules.[15] Consequently, both studies conclude that $CpZr(NMe_2)_3$ reacts with the surface to form $-ZrCp^*$, where the asterisk denotes the surface species. However, this conclusion does not agree with the experiment, which expected a Cp per two Zr atoms.[12] Since the models mimic OH-passivated Si or SiO_2, the mechanism they studied would represent the initial stage of the ALD process. Furthermore, the studies did not consider the reactions that release the Cp ligand. No study has combined *in situ* characterization experiments and theoretical studies to gain a deeper understanding of the ALD process.

In this study, we investigated the surface reactions of $CpZr(NMe_2)_3$ precursor during the ALD of ZrO_2 by combining *in situ* QCM experiments and DFT calculations. First, *in situ* QCM analysis was conducted to examine the surface species after the precursor dose. O_3 was selected as the oxygen source due to shorter purge times than H_2O[16] and better step coverage than O_2 plasma.[17] Next, DFT calculations were performed to investigate the surface reactions of $CpZr(NMe_2)_3$ on ZrO_2. The ZrO_2 slab model previously employed in the DFT study using $Zr(NMe_2)_4$[18] was also utilized in the present study. The adsorption, reaction, and activation energies were calculated for the three successive surface reactions of $CpZr(NMe_2)_3$ with ZrO_2. Furthermore, the atomistic geometries of the transition states were investigated and discussed. Finally, based on the results from the *in situ* QCM and DFT studies, the final chemisorbed species was predicted and compared with the results for $Zr(NMe_2)_4$ in the previous study.

Materials and methods

Experimental methods

ZrO_2 films were grown using a hot-wall ALD reactor (iOV-fX2, ISAC Research Co. Ltd., Republic of Korea), and the film growth was monitored in real-time using a QCM system (SQM-160, INFICON, Switzerland) with a $GaPO_4$ crystal resonator (R-30, Piezocrystal, Germany). The principles of *in situ* QCM measurements were initially established by Rocklein *et al.*[19] and Sauerbrey *et al.*[20] Further details regarding the methods and conditions were described in another publication.[21] The canister containing $CpZr(NMe_2)_3$ (Hansol Chemical Co. Ltd., Republic of Korea) was maintained at 50 °C, and the precursor vapor was supplied in conjunction with Ar carrier gas (100 sccm). An ozone-oxygen mixture generated by an ozone generator (LAB-II, Ozonetech Co., Republic of Korea) was used as a co-reactant. The pulse times of $CpZr(NMe_2)_3$ and O_3 were 7 s and 60 s, respectively. Ar gas served as the purge gas between precursor and reactant pulses. The process pressure was 1 torr. The average $\Delta f_0/\Delta f_1$ ratio was obtained from the examination during 17 ALD cycles.

Computational methods

The $Dmol^3$ module in Material Studio 7.0 (BIOVIA, USA)[22,23] was utilized for DFT calculations. The generalized gradient approximation and the Perdew–Burke–Ernzerhof exchange–correlation functional[24] were employed with a numerical basis set of double numerical polarization 4.4. The core electrons of Zr atoms were treated with the DFT semi-core potential,[25] and the DFT-D2 dispersion correction density functional was applied.[26,27] The electron configurations for Zr, O, N, C, and H elements are as follows: Zr [Kr] 5s2 4d2, O [He] 2s2 2p4, N [He] 2s2 2p3, C [He] 2s2 2p2, and H 1s1. The effective core treatment was employed for Zr only. The convergence threshold and the thermal smearing were 1×10^{-5} Ha and 9×10^{-4} Ha, respectively. The Monkhorst–Pack scheme was implemented with a K-point grid sampling of $2 \times 2 \times 1$ for the irreducible Brillouin zone. The convergence tolerance parameters for geometry optimization included a maximum displacement of 0.005 Å, a total energy change of 10^{-5} Ha, and an atomic force of 2×10^{-3} Ha Å^{-1}. The complete linear-quadratic synchronous transit (LST-QST) or QST method was employed to determine the transition state[28] with a root mean square (RMS) atomic force threshold of 0.002 Ha Å^{-1}. The details of the transition state search method have been previously discussed in another publication.[29]

The substrate model that was previously used in our research was also employed in this study.[18] Fig. 1 shows a 2×2 supercell slab model of monoclinic ZrO_2 (−111). The slab consists of 32 Zr, 72 O, and 16 H atoms. The top and bottom layers were passivated with eight OH groups, resulting in a surface OH density of 4.5 nm^{-2}. The bottom half was fixed, while the top half was relaxed for all DFT calculations.

For each reaction path, the reactant (**R**), product (**P**), and transition states (**TS**) were established. Additionally, the unbound reactant (**UR**) state, representing a system devoid of interaction between the precursor molecule and the substrate, was considered for the initial step of the chemisorption process. The energy of the **UR** state was calculated as the sum of the substrate energy ($E_{substrate}$) and the isolated precursor energy ($E_{precursor}$). The **R1** state represents the physisorption of the Zr precursor, whereas **R2** and **R3** are the states where the first and second byproducts are removed, respectively.
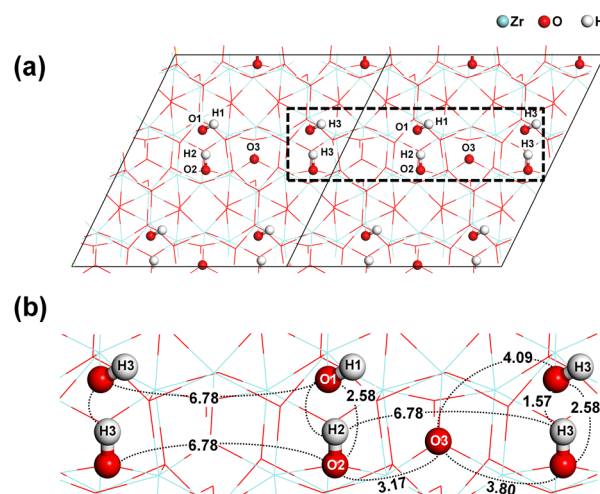

Fig. 1 Schematic illustration of (a) the monoclinic ZrO_2 (−111) slab model and (b) the reaction sites considered for the chemisorption of Zr precursor. Interatomic distances are given in Å.

The product states with one, two, and three Zr–O bonds are **P1**, **P2**, and **P3**, respectively. **TS1**, **TS2**, and **TS3** are transition states. The physisorption energy (E_{phy}), reaction energy (ΔE_n), and activation energy (E_{An}) were defined as follows:

$$E_{phy} = E_{R1} - (E_{substrate} + E_{precursor}) \qquad (1)$$

$$\Delta E_n = E_{Pn} - E_{Rn} \qquad (2)$$

$$E_{An} = E_{TSn} - E_{Rn} \qquad (3)$$

where E_{Rn}, E_{Pn}, and E_{TSn} are the system energies of **R**, **P**, and **TS** of the nth ligand release reaction.

The bond dissociation energy (BDE) was calculated using the same methodology employed in our previous publication.[18] The ZrO$_2$ slab was used to calculate the BDE of Zr–O and O–H, while the Zr precursor molecule was used for calculating the BDE of Zr–N.

Results and discussion

QCM analysis

To investigate the reaction mechanism at temperatures representative of a genuine ALD process, we examined the temperature at which the precursor thermal decomposition is not observed. Fig. 2 shows the resonance frequency change when only the CpZr(NMe$_2$)$_3$ pulse and Ar purge are repeated in the temperature range of 230 °C to 330 °C without O$_3$ supply. At 230 °C, the frequency showed a decrease during the initial cycles due to precursor chemisorption but remained nearly constant during the subsequent cycles. This suggests the self-limiting chemisorption of the precursor. Conversely, at 250 °C and above, the frequency continued to decrease with the number of cycles, indicating the mass increase due to thermal decomposition of the precursor. Therefore, the ALD process temperature was determined to be 230 °C for the QCM analysis of this work.

Fig. 3 shows the typical change in QCM resonance frequency that occurs by alternating the supply of CpZr(NMe$_2$)$_3$ and O$_3$. The frequency change during one ALD cycle was 4.2 Hz, which corresponds to the GPC of 0.55 Å, assuming the film density of
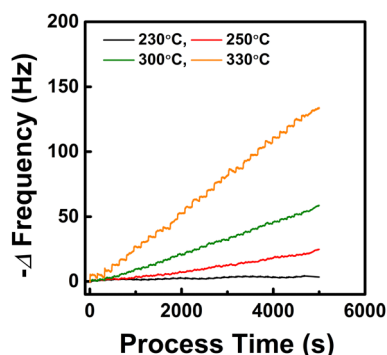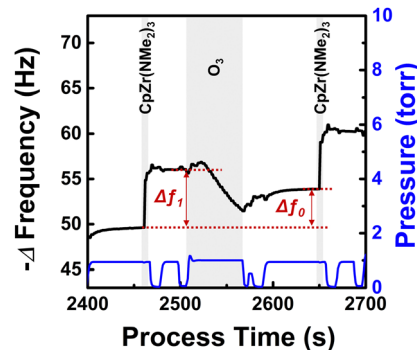

Fig. 3 Change in resonance frequency throughout the ZrO$_2$ ALD process at 230 °C. CpZr(NMe$_2$)$_3$ and O$_3$ were alternatingly supplied with pulse times of 7 s and 60 s, respectively.

4.86 g cm^{-3}.[30] The resonance frequency decrease observed during the CpZr(NMe$_2$)$_3$ pulse is primarily attributed to a mass increase by precursor chemisorption. In contrast, the frequency increase during the O$_3$ pulse is due to a mass decrease by the combustion reaction, which forms an oxide film. Δf_1 denotes the frequency change observed during the precursor pulse, while Δf_0 represents the frequency change observed throughout a complete cycle. The $\Delta f_0/\Delta f_1$ values exhibited a nearly constant ratio of 0.64 ± 0.03.

For the first half-cycle of the ALD process, the reactions of the Cp and NMe$_2$ ligands of CpZr(NMe$_2$)$_3$ with the hydroxyl groups on ZrO$_2$ were assumed to occur, resulting in the release of HCp and HNMe$_2$, respectively. The reaction equation is as follows:

$$(x + y)\text{–OH}_{(s)}^* + \text{CpZr(NMe}_2)_{3(g)}$$
$$\rightarrow (\text{–O–})_{(x+y)}\text{Cp}_{1-x}\text{Zr(NMe}_2)_{3-y(s)}^* + x\text{HCp}_{(g)} + y\text{HNMe}_{2(g)} \qquad (4)$$

where the variables x and y represent the number of Cp and NMe$_2$ released, respectively. Subsequently, the $\Delta f_0/\Delta f_1$ ratios for all potential integer values of x and y were estimated by eqn (5) in accordance with the methodology proposed by Matero et al.[31]

$$\frac{\Delta f_0}{\Delta f_1} = \frac{m_0}{m_1} = \frac{M(\text{ZrO}_2)}{M[\text{CpZr(NMe}_2)_3] - xM(\text{HCp}) - yM(\text{HNMe}_2)} \qquad (5)$$

where m_0 and m_1 denote the mass changes observed throughout a complete cycle and during the precursor pulse, respectively. M represents the molecular weight (g mol^{-1}). The estimated $\Delta f_0/\Delta f_1$ ratio most closely approximating 0.64 was 0.67 with x and y of 0 and 2, respectively, as shown in Table 1. Therefore, it can be suggested that CpZr(NMe$_2$)$_3$ underwent a reaction with the surface, resulting in the release of two HNMe$_2$ molecules, forming –O$_2$ZrCp(NMe$_2$)*.

DFT calculations

DFT simulations were conducted to investigate the surface reactions of CpZr(NMe$_2$)$_3$ on zirconium oxide. The simulation involved three successive ligand exchange reactions between

Fig. 2 Resonance frequency change resulting from repeated CpZr(NMe$_2$)$_3$ pulses and Ar purges in the absence of the O$_3$ supply. Process temperature was varied to identify the onset of the thermal decomposition of the precursor.
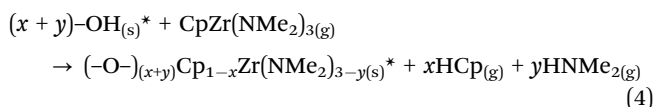
Table 1 The $\Delta f_0/\Delta f_1$ ratios estimated by eqn (5) for all potential integer combinations of the number of Cp and NMe$_2$ ligands released from a CpZr(NMe$_2$)$_3$ molecule during the first half-cycle of ZrO$_2$ ALD

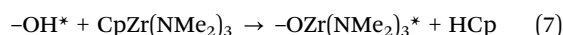| Number of Cp released (x)	Number of NMe$_2$ released (y)	Estimated $\Delta f_0/\Delta f_1$
0	0	0.46
0	1	0.54
0	2	0.67
0	3	0.86
1	0	0.59
1	1	0.75
1	2	1.00
1	3	1.52

Cp or NMe$_2$ of CpZr(NMe$_2$)$_3$ and the surface hydroxyl groups of ZrO$_2$. Since CpZr(NMe$_2$)$_3$ is a heteroleptic compound, three different initial orientations of the CpZr(NMe$_2$)$_3$ molecule were considered. In addition, two distinct paths for the release of HNMe$_2$ or HCp as byproducts were considered for each step of the surface reactions. These are illustrated in Fig. 4. **P**n**a** and **P**n**b** represent the product states after the nth surface reaction, releasing HNMe$_2$ or HCp, respectively. **R**n represents the reactant state for the nth reaction. In **R1α**, one Cp and two NMe$_2$ ligands face the substrate, while in **R1β**, three NMe$_2$ ligands face the substrate. In **R1γ**, only the Cp ligand faces the substrate. **R2** and **R3** were prepared by removing HNMe$_2$ from **P1a** and **P2a**, respectively. Upon the removal of HCp, **P1b** and **P2b** become identical to **R2** and **R3** in our previous publication with Zr(NMe$_2$)$_4$.[18] Consequently, the subsequent surface reactions from **P1b** and **P2b** are repetitions of the previous publication and were not considered in this paper.

Fig. 5 shows the energy diagrams of the first ligand exchange reaction of CpZr(NMe$_2$)$_3$, from **UR** to **P1a** or **P1b** *via* **R1α**, **R1β**, or **R1γ**. The adsorption energies of CpZr(NMe$_2$)$_3$ were −1.31 eV, −1.11 eV, and −1.07 eV for **R1α**, **R1β**, and **R1γ**, respectively, indicating that the precursor would adsorb well on ZrO$_2$. The reaction from **R1** to **P1a**, releasing HNMe$_2$, was exothermic, with the reaction energy, ΔE_{1a}, of −0.62 eV to −0.86 eV.

The E_{A1a} values, representing the activation energy for three reaction paths from **R1** to **P1a**, were relatively low at 0.22 eV in **TS1αa**, 0.19 eV in **TS1βa**, and 0.94 eV in **TS1γa**. **TS1αa**, **TS1βa**, and **TS1γa** represent the transition states between **R1α**, **R1β**, and **R1γ** and **P1a**. However, the reaction from **R1** to **P1b**, which releases HCp, was endothermic, with ΔE_{1b} values of 0.10–0.34 eV. The E_{A1b} of the paths from **R1** to **P1b** ranged from 1.66 eV to 3.98 eV. The change in entropy is relatively small because the reaction byproduct remains on the surface. Therefore, **P1a** paths are favored over **P1b** paths due to low activation energies. These results also indicate that the activation energies can vary depending on the initial orientation of the CpZr(NMe$_2$)$_3$ molecule.

The energy diagram for the three successive ligand exchange reactions of CpZr(NMe$_2$)$_3$ on the ZrO$_2$ surface is illustrated in Fig. 6. For the first reaction, the paths from the **R1α** shown in Fig. 5 were employed in Fig. 6 due to the lowest energy values. For all reactions, the pathways releasing HCp were endothermic and exhibited higher E_A values than those releasing HNMe$_2$. It can, therefore, be postulated that the surface reactions proceed through the HNMe$_2$-releasing pathways. The desorption processes of HNMe$_2$ from the product states in Fig. 6 were endothermic. However, **P1**, **P2**, or **P3** would be transformed into **R2**, **R3**, and **UP** at ALD process temperatures because the desorption processes were spontaneous due to the entropy increase at temperatures above 0 °C in the previous study.[18]

Fig. 7 presents the atomistic structural changes during the reaction from **R1** to **P1**. The following equations can describe the two paths for this reaction:

$$-OH^* + CpZr(NMe_2)_3 \rightarrow -OZrCp(NMe_2)_2{}^* + HNMe_2 \quad (6)$$

$$-OH^* + CpZr(NMe_2)_3 \rightarrow -OZr(NMe_2)_3{}^* + HCp \quad (7)$$

The formation of **P1a** by eqn (6) was exothermic due to the bond formation of Zr–O1 (5.72 eV) and N–H (3.97 eV), despite the bond dissociation of Zr–N (3.64 eV) and O1–H1 (5.13 eV).[18,32] In contrast, the formation of **P1b** by eqn (7) was
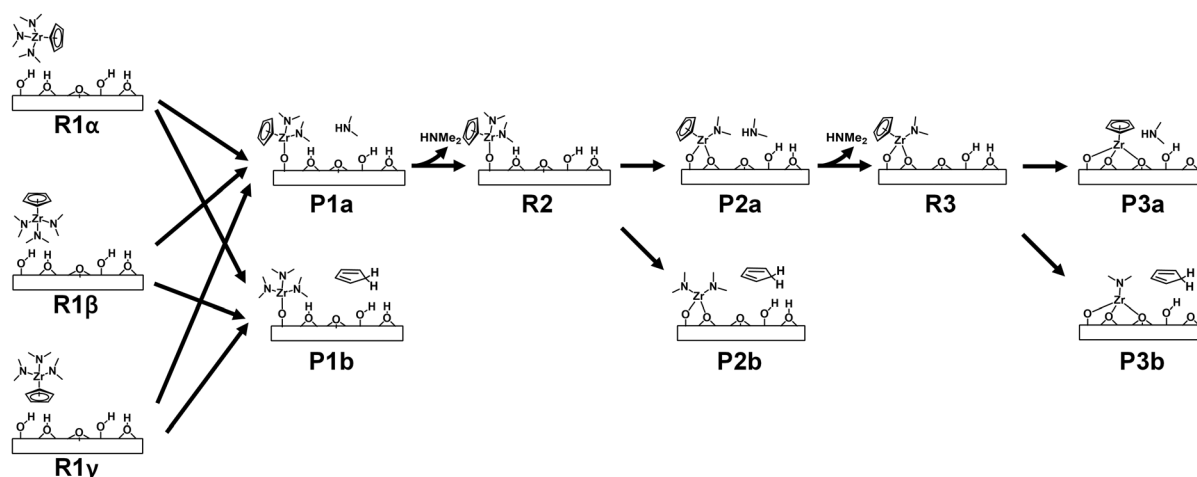

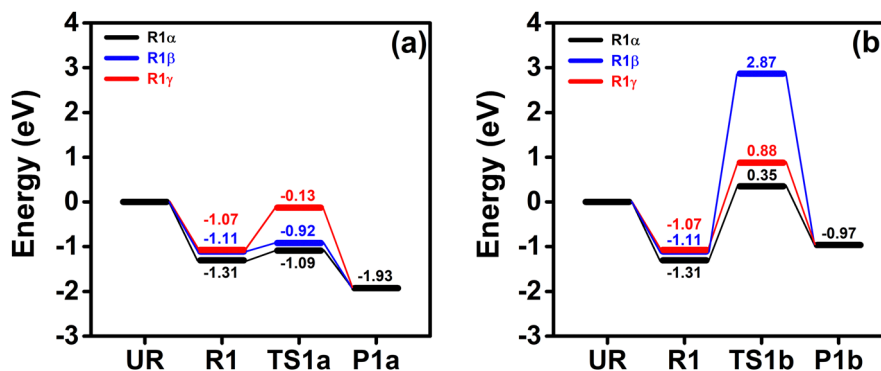**Fig. 4** Schematic of the multiple paths of surface reactions of CpZr(NMe$_2$)$_3$ on the ZrO$_2$ substrate.

Fig. 5 Energy diagrams for the first reaction of $CpZr(NMe_2)_3$ from three reactant states, **R1α**, **R1β**, and **R1γ**, to two product states, (a) **P1a** and (b) **P1b**.
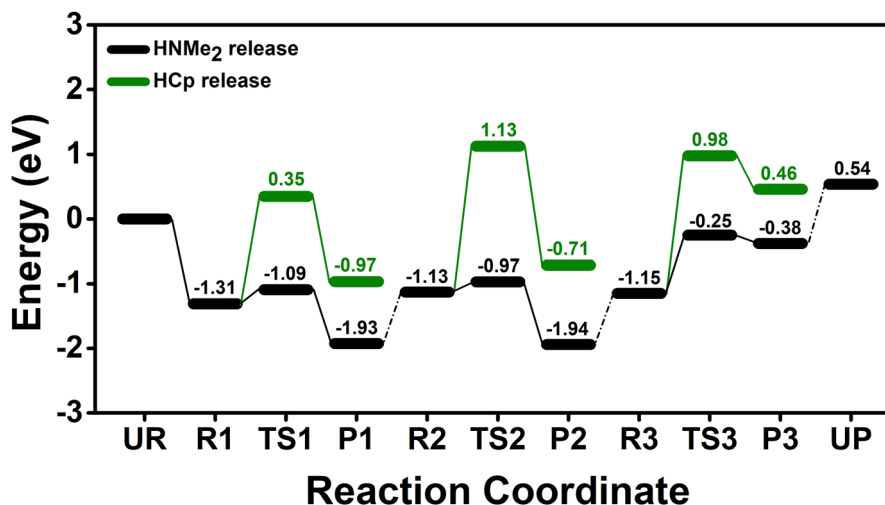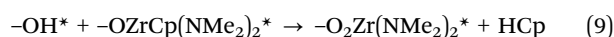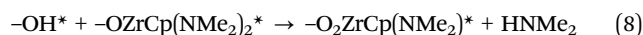

Fig. 6 Energy diagrams for the surface reactions of $CpZr(NMe_2)_3$ on ZrO_2. The **Pna** states are the product states resulting from the nth surface reaction with the release of $HNMe_2$, while the **Pnb** states are the product states arising from the release of HCp.

endothermic. In comparison to eqn (6), the Zr–Cp bond (4.29 eV), which is stronger than the Zr–N bond, was dissociated, while the H–Cp bond (3.56 eV), which is weaker than the N–H bond, was newly formed in eqn (7).

In the paths leading to the formation of **P1a**, the N1–H1 bond was formed without dissociation of any bond in all **TS1a** states. This resulted in relatively low activation energy values, as shown in Fig. 5, although the Zr–N1 bond was extended. Since the Zr–N1 bond was the shortest at 2.27 Å in **TS1αa**, the activation energy of the path from **R1α** was the lowest at 0.22 eV. In contrast, the paths leading to the formation of **P1b** involve the dissociation of the Cp–Zr bond or the loss of aromaticity of Cp in **TS1b** states, resulting in relatively high activation energies, as shown in Fig. 5. In **TS1αb**, the H1 atom was dissociated from O to migrate to Cp and form the H1–Cp bond, which resulted in the loss of aromaticity. The Zr-η^1-CpH bond in **TS1αb** is considerably weaker than the Zr-η^5-Cp bond in the **R1α** states, resulting in an activation energy of 1.66 eV, despite the formation of the Zr–O1 bond. In **TS1βb** and **TS1γb**, higher activation energies of 3.98 and 1.95 eV were obtained

due to the dissociation of the Cp–Zr bond despite the formation of the Zr–O1 or H1–Cp bond.

Fig. 8 shows the atomistic structural changes for the reaction from **R2** to **P2**. The following equations describe the two paths for this reaction:

$$-OH^* + -OZrCp(NMe_2)_2^* \rightarrow -O_2ZrCp(NMe_2)^* + HNMe_2 \quad (8)$$

$$-OH^* + -OZrCp(NMe_2)_2^* \rightarrow -O_2Zr(NMe_2)_2^* + HCp \quad (9)$$

The formation of **P2a** by eqn (8) was exothermic, while the formation of **P2b** by eqn (9) was endothermic. The exothermicity or endothermicity of eqn (8) and (9) are comparable to eqn (6) and (7) because the dissociated or formed bonds are the same in both cases.

The atomistic structure of **TS2a** was analogous to that of **TS1a**, with the N2–H2 bond formed and the Zr–N2 bond elongated from 2.09 Å to 2.22 Å, resulting in a low activation energy of 0.16 eV. **TS2b**, similar to **TS1αb**, also lost the aromaticity of Cp resulting from the migration of H2 to Cp. However,
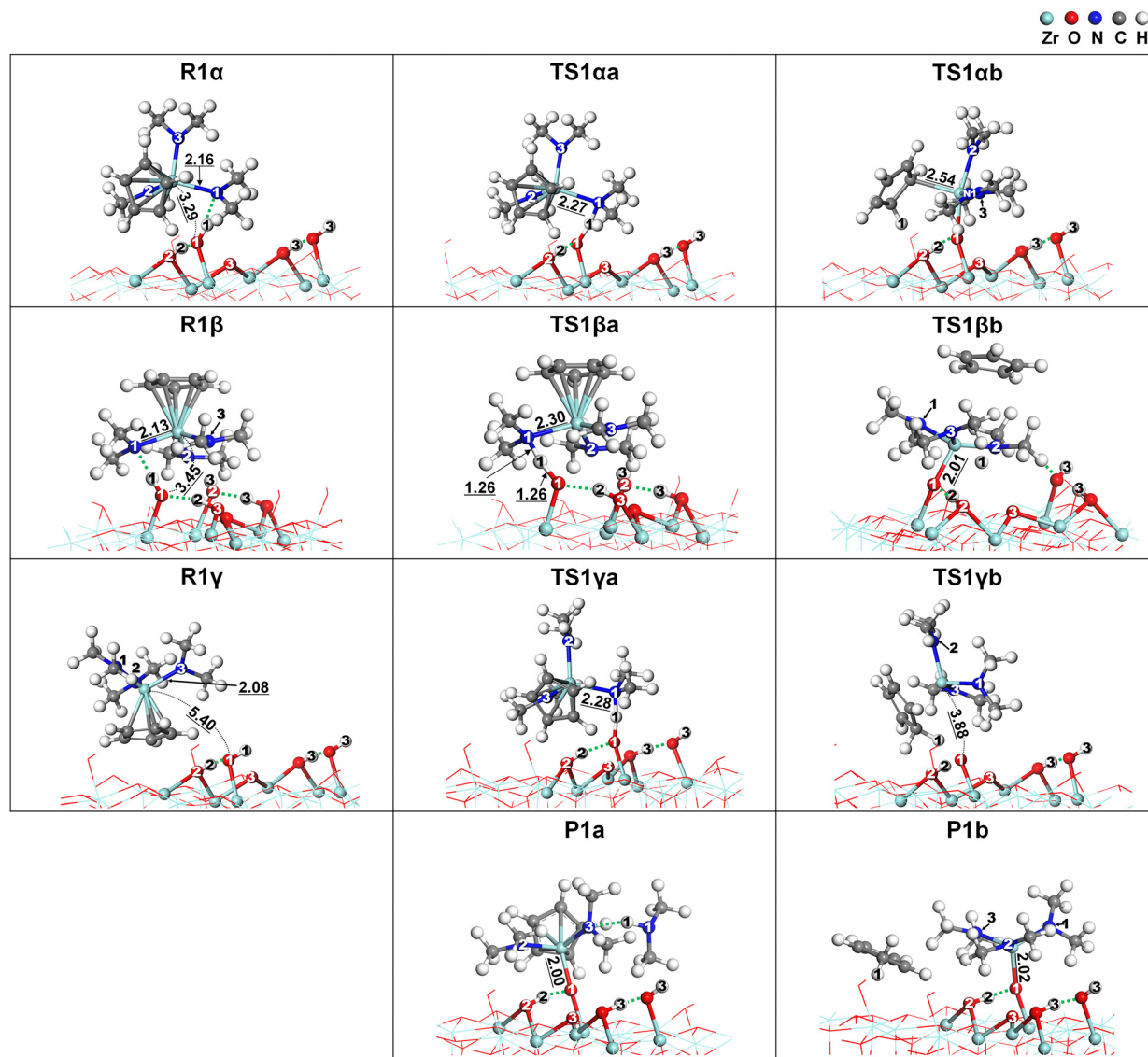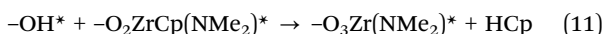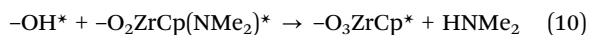
Fig. 7 The atomistic structural changes for the paths from three reactant states, **R1α**, **R1β**, and **R1γ**, to two product states, **P1a** and **P1b**. The dotted lines indicate hydrogen bonds. Bond lengths are given in Å.

it showed a relatively high activation energy of 2.26 eV because the Zr–O2 bond was not yet formed.

Fig. 9 shows the atomistic structural changes that occur during the reaction from **R3** to **P3**. Two paths were also assumed as follows:

$$-\text{OH}^* + -\text{O}_2\text{ZrCp(NMe}_2)^* \rightarrow -\text{O}_3\text{ZrCp}^* + \text{HNMe}_2 \quad (10)$$

$$-\text{OH}^* + -\text{O}_2\text{ZrCp(NMe}_2)^* \rightarrow -\text{O}_3\text{Zr(NMe}_2)^* + \text{HCp} \quad (11)$$

In **R3**, the surface chemical species $\text{O}_2\text{ZrCp(NMe}_2)^*$ has Cp and NMe_2 in opposite directions around the Zr atom, as shown in Fig. 9. In contrast to the reactions to **P1** or **P2**, both paths to **P3** were endothermic, with ΔE_{3a} of 0.77 eV and ΔE_{3b} of 1.61 eV. The cleavage of the subsurface O3–Zr bond of both **P3a** and **P3b** in Fig. 9 can explain the observed endothermicity.

The activation energy for the path represented by eqn (10), which releases HNMe_2, was 0.90 eV, which is higher than those of eqn (6) and (8) in the reactions to **P1** and **P2**. In **TS3a**, the Zr–O3 and Zr–N3 bonds were elongated, and H3b migrated from $-\text{OH3b}^*$ to the neighboring $-\text{OH3a}^*$ to form $-\text{OH}_2^*$. The activation energy for eqn (11), which releases HCp, was 2.13 eV. In **TS3b**, the Zr–Cp bond was dissociated, and H3b migrated from $-\text{OH3b}^*$ to form HCp. The Zr–O3 bond has not yet been formed. Consequently, the reaction to **P3** would be energetically unfavorable in contrast to the reactions to **P1** and **P2**.

The above DFT calculations predict that $\text{CpZr(NMe}_2)_3$ reacts with ZrO_2 to form $\text{O}_2\text{ZrCp(NMe}_2)^*$ surface species, which agrees with the results of the QCM analysis. The surface reaction of $\text{CpZr(NMe}_2)_3$ is expected to proceed along paths that release two HNMe_2 molecules one at a time, while the release of HCp is expected to be unfavorable. Therefore, the surface reactions of
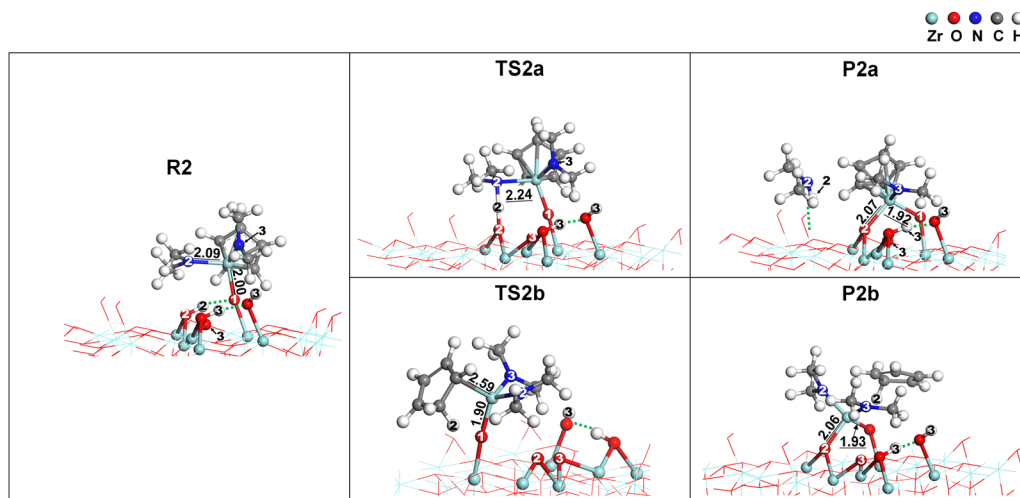
Fig. 8 The atomistic structural changes for the paths from **R2** to two product states, **P2a** and **P2b**. The dotted lines indicate hydrogen bonds. Bond lengths are given in Å.
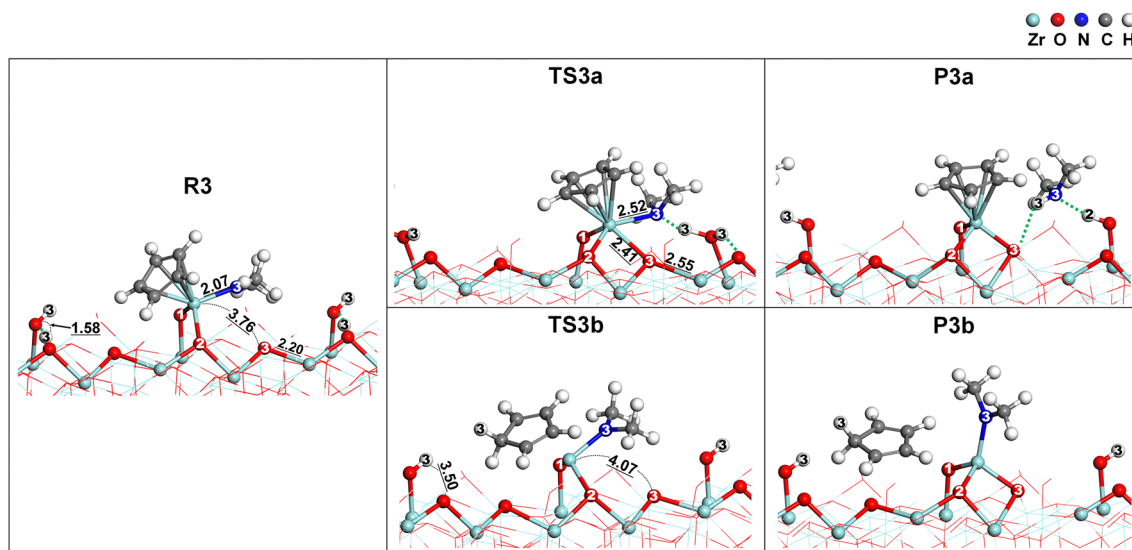

Fig. 9 The atomistic structural changes for the paths from **R3** to two product states, **P3a** and **P3b**. The dotted lines indicate hydrogen bonds. Bond lengths are given in Å.

Table 2 Comparison of surface reactions of $CpZr(NMe_2)_3$ and $Zr(NMe_2)_4$

Reaction step	Energy (eV)	$Zr(NMe_2)_4$ [18]	$CpZr(NMe_2)_3$ (this study)	
			HNMe$_2$ release	HCp release
Physisorption	E_{ads}	−1.16	−1.31	−1.31
1st reaction	ΔE_1	−0.68	−0.62	0.34
	E_{A1}	0.19	0.22	1.66
2nd reaction	ΔE_2	−1.06	−0.81	0.42
	E_{A2}	0.24	0.16	2.26
3rd reaction	ΔE_3	0.64	0.77	1.61
	E_{A3}	0.75	0.90	2.13

$CpZr(NMe_2)_3$, a heteroleptic precursor, were similar to those of $Zr(NMe_2)_4$, a homoleptic precursor reported in our previous publication.[18] Table 2 compares the calculated energy values for the surface reaction of $Zr(NMe_2)_4$ and $CpZr(NMe_2)_3$. For the

HNMe$_2$ releasing paths, $CpZr(NMe_2)_3$ exhibited similar reaction and activation energy values to those of $Zr(NMe_2)_4$. The slight difference in energy values can be explained by the difference in BDE in the two compounds. For example, the E_{A2} of 0.16 eV for $CpZr(NMe_2)_3$ is lower than 0.24 eV for $Zr(NMe_2)_4$ due to the lower BDE of the Zr–N bond in $CpZr(NMe_2)_3$ compared to that in $Zr(NMe_2)_4$. The strong Cp–Zr bond results in a BDE of the Zr–N bond of 3.64 eV in $CpZr(NMe_2)_3$, which is lower than the BDE of 3.74 eV for $Zr(NMe_2)_4$.

Conclusions

The reaction mechanism of ALD ZrO_2 using $CpZr(NMe_2)_3$ was investigated through the use of *in situ* QCM and DFT. The QCM

analysis yielded a $\Delta f_0/\Delta f_1$ ratio of 0.64 ± 0.03 at 230 °C, indicating that one Cp ligand and one NMe_2 ligand remained on the surface per $CpZr(NMe_2)_3$ molecule. A DFT calculation was conducted to simulate the successive ligand exchange reactions between $CpZr(NMe_2)_3$ and $-OH$ terminated ZrO_2. The paths releasing the first two NMe_2 ligands were exothermic, with low activation energy values of 0.22 eV and 0.16 eV. In contrast, the release of the third NMe_2 ligand was endothermic and exhibited a high activation energy of 0.90 eV. The paths releasing the Cp ligand were all endothermic and exhibited high activation energies of 1.66–2.26 eV. Consequently, the resulting surface species would be $O_2ZrCp(NMe_2)^*$, which is consistent with the QCM analysis.

Author contributions

H.-L. Kim: conceptualization, data curation, formal analysis, methodology, project administration, validation, visualization, writing – original draft. O. Kim: data curation, formal analysis, investigation, methodology, validation, visualization, writing – original draft. Yong Richard Sriwijaya: formal analysis, investigation, methodology, visualization. Khabib Khumaini: validation, writing – review & editing. Romel Hidayat: conceptualization, methodology, writing – review & editing. Won-Jun Lee: conceptualization, funding acquisition, project administration, resources, supervision, validation, writing – review & editing.

Data availability

The data supporting this article have been included in the ESI.†

Conflicts of interest

There are no conflicts to declare.

Acknowledgements

Notes and references

1 R. Katamreddy, Z. Wang, V. Omarjee, P. V. Rao, C. Dussarrat and N. Blasco, ECS Trans., 2009, 25, 217–230.
2 T. Blanquart, J. Niinistö, M. Gavagnin, V. Longo, V. R. Pallem, C. Dussarrat, M. Ritala and M. Leskelä, Chem. Mater., 2012, 24, 3420–3424.
3 K. Xu, A. P. Milanov, H. Parala, C. Wenger, C. Baristiran-Kaynak, K. Lakribssi, T. Toader, C. Bock, D. Rogfrealla, H. W. Becker, U. Kunze and A. Devi, Chem. Vap. Deposition, 2012, 18, 27–35.
4 M. Kaipio, T. Blanquart, M. Banerjee, K. Xu, J. Niinistö, V. Longo, K. Mizohata, A. Devi, M. Ritala and M. Leskelä, Chem. Vap. Deposition, 2014, 20, 209–216.
5 S. C. Buttera, P. Rouf, P. Deminskyi, N. J. O'Brien, H. Pedersen and S. T. Barry, Inorg. Chem., 2021, 60, 11025–11031.
6 J.-H. Baek, W.-H. Choi, H. Kim, S. Cheon, Y. Byun, W. Jeon and J.-S. Park, Ceram. Int., 2021, 47, 29030–29035.
7 H. Choi, C. Park, S. K. Lee, J. Y. Ryu, S. U. Son, T. Eom and T.-M. Chung, ACS Omega, 2023, 8, 43759–43770.
8 J. Niinistö, K. Kukli, M. Kariniemi, M. Ritala, M. Leskelä, N. Blasco, A. Pinchart, C. Lachaud, N. Laaroussi, Z. Wang and C. Dussarrat, J. Mater. Chem., 2008, 18, 5243–5247.
9 J. Niinistö, T. Blanquart, S. Seppälä, M. Ritala and M. Leskelä, ECS Trans., 2014, 64, 221–232.
10 T. Blanquart, J. Niinistö, M. Ritala and M. Leskelä, Chem. Vap. Deposition, 2014, 20, 189–208.
11 S. Kim, R. Hidayat, H. Roh, J. Kim, H.-L. Kim, K. Khumaini, M. Park, J.-H. Seok, J. W. Park and W.-J. Lee, J. Mater. Chem. C, 2022, 10, 6696–6709.
12 L. Aarik, H. Alles, A. Aidla, T. Kahro, K. Kukli, J. Niinistö, H. Mändar, A. Tamm, R. Rammula, V. Sammelselg and J. Aarik, Thin Solid Films, 2014, 565, 37–44.
13 J.-S. Jung, S.-K. Lee, C.-S. Hong, J.-H. Shin, J.-M. Kim and J.-G. Kang, Thin Solid Films, 2015, 589, 831–837.
14 T. T. Van Ngoc, D. Jang, E. Jung, H. Noh, J. Moon, D.-S. Kil, S.-W. Chung and B. Shong, J. Phys. Chem. C, 2022, 126, 18090–18099.
15 A. R. Choi, S. Seo, S. Kim, D. Kim, S.-W. Ryu, W.-J. Lee and I.-K. Oh, Appl. Surf. Sci., 2023, 624, 157104.
16 X. Liu, S. Ramanathan, A. Longdergan, A. Srivastava, E. Lee, T. E. Seidel, J. T. Barton, D. Pang and R. G. Gordon, J. Electrochem. Soc., 2005, 152, G213.
17 S. M. George, Chem. Rev., 2010, 110, 111.
18 R. Hidayat, H.-L. Kim, Y. R. Sriwijaya, K. Khumaini and W.-J. Lee, Surf. Interfaces, 2024, 50, 104480.
19 M. N. Rocklein and S. M. George, Anal. Chem., 2003, 75, 4975–4982.
20 G. Sauerbrey, Verwendung von Schwingquarzen zur Wagung dunner Schichten und zur Mikrowagung, Z. Phys., 1959, 155, 206–222.
21 K. Khumaini, H. Roh, H. Han, H.-L. Kim, H. S. Kim, J.-H. Seok, J. W. Park and W.-J. Lee, Appl. Surf. Sci., 2023, 615, 156340.
22 B. Delley, J. Chem. Phys., 1990, 92, 508–517.
23 B. Delley, J. Chem. Phys., 2000, 113, 7756–7764.
24 J. P. Perdew, K. Burke and M. Ernzerhof, Phys. Rev. Lett., 1996, 77, 3865.
25 B. Delley, Phys. Rev. B: Condens. Matter Mater. Phys., 2002, 66, 1–9.
26 S. Grimme, J. Comput. Chem., 2006, 27, 1787–1799.
27 E. R. McNellis, J. Meyer and K. Reuter, Phys. Rev. B: Condens. Matter Mater. Phys., 2009, 80, 205414.
28 N. Govind, M. Petersen, G. Fitzgerald, D. King-Smith and J. Andzelm, Comput. Mater. Sci., 2003, 28, 250–258.

29 K. Khumaini, R. Hidayat, T. R. Mayangsari, T. Chowdhury, H.-L. Kim, S.-I. Lee and W.-J. Lee, *Appl. Surf. Sci.*, 2002, **585**, 152750.

30 D. Ceresoli and D. Vanderbilt, *Phys. Rev. B: Condens. Matter Mater. Phys.*, 2006, **74**, 125108.

31 R. Matero, A. Rahtu and M. Ritala, *Chem. Mater.*, 2001, **13**, 4506–4511.

32 Y. Choi, H. Son, K. Khumaini, H. Han, H. Roh, H.-L. Kim, S.-I. Lee and W.-J. Lee, *J. Mater. Chem. C*, 2022, **10**, 17377–17385.